

How a G Protein Binds a Membrane*

Received for publication, March 26, 2004, and in revised form, May 26, 2004
Published, JBC Papers in Press, June 1, 2004, DOI 10.1074/jbc.M403404200

Zhixian Zhang, Thomas J. Melia‡, Feng He, Ching Yuan§, Amy McGough¶, Michael F. Schmid, and Theodore G. Wensel||

From the Verna and Marrs McLean Department of Biochemistry and Molecular Biology, Baylor College of Medicine, Houston, Texas 77030

Heterotrimeric G proteins interact with receptors and effectors at the membrane-cytoplasm interface. Structures of soluble forms have not revealed how they interact with membranes. We have used electron crystallography to determine the structure in ice of a helical array of the photoreceptor G protein, transducin, bound to the surface of a tubular lipid bilayer. The protein binds to the membrane with a very small area of contact, restricted to two points, between the surface of the protein and the surface of the lipids. Fitting the x-ray structure into the membrane-bound structure reveals one membrane contact near the lipidated G γ C terminus and G α N terminus, and another near the G α C terminus. The narrowness of the tethers to the lipid bilayer provides flexibility for the protein to adopt multiple orientations on the membrane, and leaves most of the G protein surface area available for protein-protein interactions.

G proteins mediate signal transduction pathways on the membranes of virtually all eukaryotic cells. In the inactive, GDP-bound, heterotrimeric state most G proteins are themselves tightly membrane associated. Activation takes place when GTP is exchanged for GDP in a complex with an integral membrane G protein-coupled receptor, which produces separated and active G α -GTP and G $\beta\gamma$ proteins. These active subunits are then free to move along the membrane and regulate their downstream effectors that may be either peripherally membrane associated (*e.g.* cGMP phosphodiesterase, phospholipase C) or integral membrane proteins (*e.g.* adenylyl cyclase and ion channels).

There have been numerous studies of G protein-membrane interactions using biochemical, functional, and mutagenic approaches. These have made it clear that membrane association and localization play a critical role in G protein function and have also revealed biochemical features of G α and G γ that are important for membrane binding. All G α subunits have one or more fatty acids added at or near their N termini, and both the

fatty acids and the amino acids in the N-terminal region are important for membrane binding (1–3). The attachment site is either an N-terminal glycine, which is linked to fatty acid, usually myristic acid, in an amide linkage, or a cysteine at position 2, which is linked to palmitic acid in a thioester linkage. The G γ subunits are proteolytically processed to leave a C-terminal methyl-esterified cysteine residue linked via a thioether to either a 15- or 20-carbon isoprenyl chain (4–8). Forms of G γ without these modifications have been studied, and they show reduced interactions with membranes and defective signaling properties (9–14).

In the crystal structures of G protein heterotrimers (15, 16) these hydrophobic modifications and their immediately adjacent amino acids are missing; however, the resolved portions of the G γ C terminus and the G α N terminus are close to one another in space, suggesting a common site for membrane insertion. The only G protein structure in which a lipid modification is present and visible is the complex of G $\beta\gamma_t$ with phosducin, in which the farnesyl group is tucked into the β -propeller blades of G β_t (17), and which has greatly diminished affinity for membranes. Another region thought to be near the membrane is the C terminus of the α subunit, because of its critical role in binding to receptors (18, 19).

A proposed membrane-binding surface for the heterotrimer was identified by adding to these constraints a criterion of electrostatic matching between positively charged or neutral regions of the protein surface and the negatively charged phospholipid (16). However, this model remains in question because studies with the retinal G protein transducin have suggested that there is no electrostatic attraction to the membrane. In fact, low ionic strength is routinely used to remove this protein from membranes, suggesting that the net electrostatic forces are actually weakly repulsive in nature (20–22). In general it is not clear that there is a strong driving force for the dehydration of the polar surfaces of both the protein and the lipid head groups required to bring about close contact between them. Thus a fundamental question about a peripheral membrane protein binding to a lipid bilayer is whether their facing surfaces interact primarily with water or with one another.

Because of the intrinsic difficulty of incorporating a membrane-protein interface into three-dimensional crystals suitable for x-ray crystallography, we have used the approach of electron crystallography to determine the structure of the G protein-membrane complex. In this approach the protein is allowed to assemble into an ordered lattice on the surface of a lipid bilayer, and electron microscopy of samples preserved in vitreous ice is used to obtain images for structural analysis. Although in most cases only low resolution structural maps are obtained from this technique, it is possible to fit high resolution structures into these maps computationally (23–26), and thus obtain information about the interactions of specific parts of the protein with the membrane.

* This work was supported in part by National Institutes of Health Grant EY07981, National Center for Macromolecular Imaging Grant RR02250, and the Welch Foundation. The costs of publication of this article were defrayed in part by the payment of page charges. This article must therefore be hereby marked "advertisement" in accordance with 18 U.S.C. Section 1734 solely to indicate this fact.

‡ Supported by Houston Area Molecular Biophysics Program Grant T32-GM08280. Present address: Memorial Sloan-Kettering Cancer Center, New York, NY 10021.

§ Present address: Dept. of Ophthalmology, University of Minnesota Medical School, Minneapolis, MN 55455.

¶ Present address: Dept. of Biological Sciences, Purdue University, West Lafayette, IN 47907-1392.

|| To whom correspondence should be addressed: Dept. of Biochemistry and Molecular Biology, Baylor College of Medicine, One Baylor Plaza, Houston, TX 77030. Tel.: 713-798-6994; Fax: 713-796-9438; E-mail: twensel@bcm.tmc.edu.

We reported previously that ordered lattices could be obtained for the photoreceptor G protein transducin either on planar monolayers (27) or tubular bilayers (28), and that the tubular structures were occasionally obtained using endogenous lipids co-purifying with the protein, although a specific mixture of synthetic lipids formed them most efficiently. Only the tubular structures, which have helical symmetry, proved to be suitable for structural analysis. We report here the results of reconstructing the protein-lipid complex and fitting of the x-ray crystal structure of the heterotrimeric G protein (16), which allow us to identify the mechanisms by which the G protein interacts with the membrane surface. In addition to revealing the G protein orientation on the membrane surface, these results suggest that electron crystallography using helical protein lattices assembled on lipid tubules may be a generally applicable approach for determining membrane orientations for peripheral proteins.

EXPERIMENTAL PROCEDURES

Reagents and Materials—Buffer A was 5 mM Tris, 0.5 mM MgCl₂, pH 7.4, 1 mM dithiothreitol. Buffer B was 20 mM MOPS,¹ 2 mM MgCl₂, pH 8.0, 50 mM NaCl, 1 mM dithiothreitol, 0.2 mM EDTA. Buffer C was 10 mM MOPS, 10 mM MgCl₂, pH 7.4, 1 mM dithiothreitol. Tube buffer was Buffer B supplemented with 5% (v/v) glycerol, 10 μM N,N,N',N'-tetrakis(2-pyridylmethyl)-ethylenediamine (TPEN, Aldrich), and 10 mM CaCl₂.

All buffers were filtered through 0.2-μm nitrocellulose filters immediately before use. Buffers used in purification also contained a small amount of solid protease inhibitor, phenylmethylsulfonyl fluoride (Roche Applied Science).

G_t was purified essentially as described (28). Briefly, crude G_t was prepared by stripping G_t from bleached, washed bovine rod outer segment membranes (ROS) with GTP and buffer A. Crude G_t was then exchanged into buffer C and purified over an high performance liquid chromatography anion exchange column (Waters DEAE-5PW), by elution with increasing NaCl. Purified protein was exchanged into buffer B and stored in 50% glycerol at -20°C. Dioleoyltrimethylammonium propane and diphytanoyl phosphatidylcholine were purchased from Avanti in CHCl₃ and stored at -80°C under argon, unless otherwise noted.

Two-dimensional Crystallization—Conditions for helical crystallization were similar to those described previously (28). G_t (0.1–0.2 mg/ml) in tube buffer with 5% (v/v) glycerol (glycerol concentration is critical for reproducible tube formation) was pipetted into clean 10-μl Teflon wells and ~1 μl of a 0.5–1 mg/ml lipid mixture (20:80 mol/mol dioleoyltrimethylammonium propane:diphytanoyl-PC) in 1:1 (v/v) chloroform:hexane was floated over the solution to form a lipid monolayer. The samples were kept in a humid environment by placing the Teflon plates on damp filter paper in glass Petri dishes at 4°C. Tubes formed in under 2 h.

Grid Preparation—Tubes were transferred by pipetting 5 μl from either the surface or the subphase onto 400-mesh copper electron microscope grids (Gilder, Ted Pella) to which a carbon-coated holey film had been applied (29, 30) so that the sample was suspended in a thin aqueous layer across the holes. For cryo-preservation of the helical tubes, excess sample was wicked off with Whatman No. 1 filter paper, and then the grid was immediately plunged into liquid ethane. Samples were stored in liquid nitrogen.

Electron Microscopy and Image Digitization—The specimen was examined on a JEOL 1200EX cryo-microscope operating at 100 kV and outfitted with a Gatan cryo-stage maintained at <-162°C (31). The images were taken at ×40,000 magnification with an electron dose of ~12 electrons/Å² and recorded on Kodak So-163 film. The film was developed in Kodak Developer D19 for 12 min at 20°C and fixed for 10 min in Kodak fixer. Images were digitized on a Zeiss SCAI microdensitometer at a step size of 3.5 Å/pixel.

Image Processing and Helical Reconstruction—Tubule images with the same diameters and long straight regions were selected visually, then the tubes were boxed and floated into a square area using the software routine Boxer in the EMAN suite (32). Inspection and preliminary identification of layer lines in computed Fourier transforms were carried out in SPECTRA (33). Images with strong symmetrical diffrac-

tion patterns and sharp layer lines were selected for further processing. Indexing was facilitated by programs that calculated a range of possible Bessel orders for each layer line, and cross-checked potential selection rules for self-consistency among all these possible Bessel orders. In addition, a test for odd *versus* even Bessel orders by examining the phases of the layer lines was performed to further narrow the choice of Bessel orders; all were found to be multiples of six. Layer line extraction and refinement as well as reconstruction by Fourier-Bessel inversion were performed with programs based on the original MRC helical reconstruction algorithms (34) updated to accommodate our image parameters and data formats. The final map was derived from both sides of 3 tubes of the same class at defocus values near 1.3 μm, with a total of 3800 heterotrimers. For each layer line, data from both sides of all three tubes were averaged after 2-fold symmetry was enforced, and data out to the first zeros of the CTF (22–23 Å) were included. The amplitude-weighted phase residual for 2-fold symmetry was 24°, calculated from all Fourier terms (not including equatorial peak) with amplitudes higher than 2% of the highest peak in the off-equatorial data for both sides of three tubes (six sides total). Inter-particle phase residuals were 28.8°, 31.3°, and 30.1°, and intra-particle (near *versus* far side) phase residuals were 34.9°, 36.0°, and 39.2°. The radial density profile was calculated by back-transformation of the equatorial line in the Fourier transform. To test for Fresnel fringe effects in this profile, an approximate contrast transfer function (CTF) amplitude correction was performed on the transform after low-pass filtering, by using a predicted CTF for the experimental defocus value with an estimate of 10% amplitude contrast. The predicted CTF was used as an inverse filter for the equatorial data in Fourier space to produce the solid curve in Fig. 3D.

Fitting of X-ray Structure into EM-derived Density Map—The reconstruction was visualized using IRIS Explorer (Numerical Algorithms Group, Ltd., Oxford, UK) with custom designed modules (35), and a single heterotrimer unit excised computationally. The coordinate file for the Gαβγ_t trimer structure determined by x-ray crystallography using Protein Data Bank code 1GOT (16) was obtained from the Protein Data Bank (RCSB (36)) and used to generate a density map at 30 Å resolution using the program PDB2MRC in the EMAN suite (32). It was fitted into the heterotrimer density of the reconstruction based on a local six-dimensional (rotation and translation) cross-correlation search using *Foldhunter* (23). The solution was independent of the initial orientation and position selected. The assignment of the best fit was judged by the maximal correlation coefficient, and confirmed by visual inspection of matching of the fitted structures. Because the data are from projection images, an ambiguity exists with respect to the handedness of the EM map determined by the arbitrary selection of the signs of the Bessel orders of the layer lines in the computed diffraction pattern. Both choices were tested, and the one giving the best fit to the x-ray structure was used. Surface representations were generated and the electrostatic potential map was colored using GRASP (37).

RESULTS

Electron Microscopy of G_t Tubules—The G_t helical crystals observed in images obtained by electron cryo-microscopy fall into multiple classes or families with a range of diameters from 430–750 Å. An image of a G_t tubule embedded in vitreous ice, from a commonly observed family with a diameter of 540 Å, is shown in Fig. 1A. The tubes formed using the conditions described under “Experimental Procedures” are generally wider than those reported previously (28), which were typically closer to 270 Å in diameter. The computed Fourier transform (Fig. 1B) of each tubule is composed of a series of sharp layer lines extending to an axial resolution of 31 Å (outlined by a *rectangle*, Fig. 1, B and C), which were indexed according to the notation (*h*, *k*; *n*), as labeled in Fig. 2, indicating lattice position (*h*, *k*) and helical start number, or Bessel order (*n*) as described (34). In addition to the family used for reconstruction, an example of which is shown in Fig. 1, we also processed several additional tubes with diameters ranging from 430–680 Å (data not shown), and found that most have a similar pattern of layer lines in their Fourier transforms, but with different spacings. This similarity indicates that essentially the same surface lattice is used to form the different diameter tubes, likely using common points of protein-protein and protein-lipid contact. This observation of multiple tube diameters based on essen-

¹ The abbreviations used are: MOPS, 4-morpholinepropanesulfonic acid; CTF, contrast transfer function.

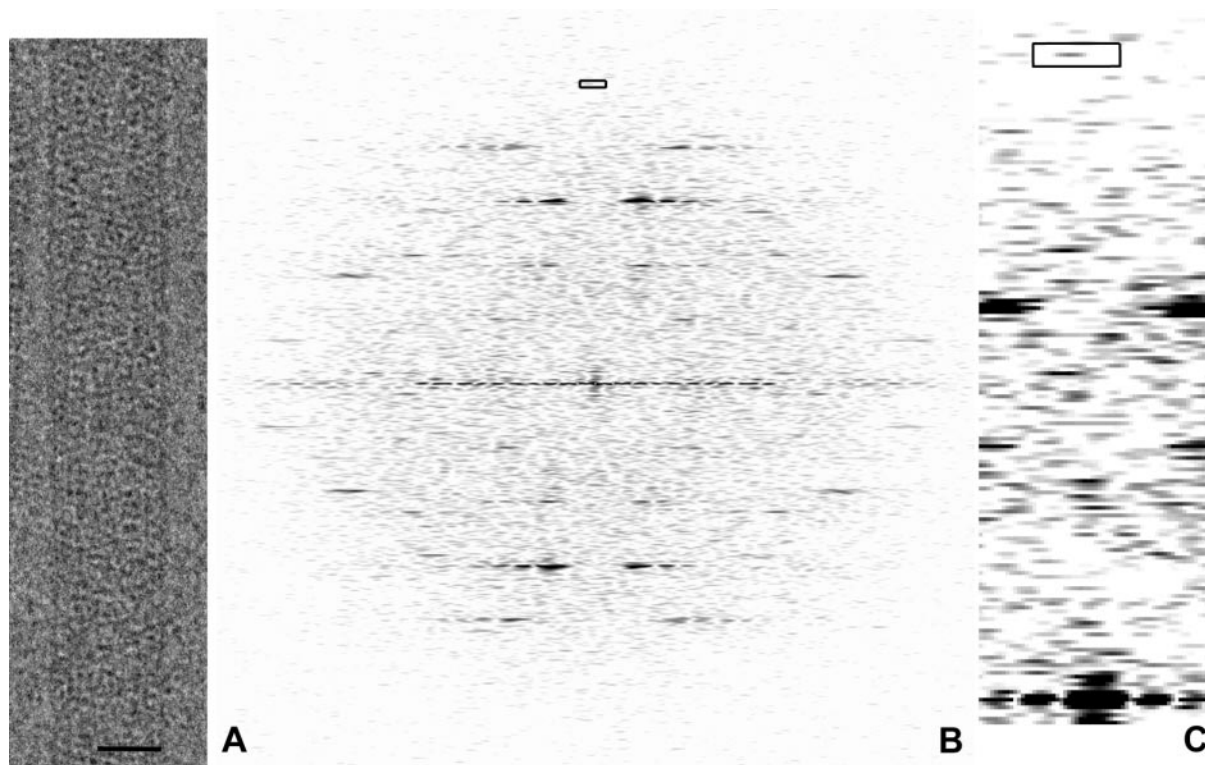


FIG. 1. **Electron micrograph and computed diffraction pattern.** *A*, electron micrograph of a G_t tube embedded in vitreous ice taken at a magnification of $\times 40,000$. The section shown is one-third the length of the tube used for reconstruction. The scale bar represents 300 Å. *B*, a computed Fourier transform. The rectangle drawn in the upper half indicates the position of a meridional layer line at a resolution of 31 Å. *C*, close-up of transform from panel *B*, with enhanced contrast.

tially identical surface lattices is a fairly common one for tubular crystals (38–41). As also observed for nicotinic acetylcholine receptor (39), sarcoplasmic reticulum Ca^{2+} -ATPase (42), and the cytochrome *bc1* complex (43), each tubule has 2-fold symmetry about an axis perpendicular to the long axis of the tube, so that the phases for the peaks in the transform are expected to be either 0° (360°) or 180° . The phase plots (Fig. 2*A*) for off-equatorial layer lines ranging from the strongest (1, 1; –6) to one of the weakest (–3, 2; 48) show good matching for most peaks with phases at amplitude maxima close to either 0° (360°) or 180° , indicating good 2-fold rotational symmetry. To evaluate the symmetry, the amplitude-weighted phase residual for 2-fold symmetry was calculated for each tube (with near and far sides averaged) from all off-equatorial Fourier terms with amplitudes higher than 2% of the highest of such terms in each transform. The phase residuals for the three tubes were 22.1° , 26.1° , and 24.4° .

Helical Reconstruction—The helical reconstruction shown in Fig. 3 was generated using merged data out to a maximum isotropic resolution of 23 Å and an axial resolution limit of 31 Å, from three tubes of the same family as the tube illustrated in Figs. 1 and 2 with a total of ~ 3800 heterotrimer units. In Fig. 3 and subsequent figures, for clarity, the map is presented with a density threshold selected to include 85% of the molecular volume of each heterotrimer. The main features of the tube are a relatively smooth continuous cylinder, consistent with a lipid bilayer, and an outer layer of globular densities of the size and shape of $G\alpha\beta\gamma_t$ heterotrimers. The arrows in the cross-sectional view shown in Fig. 3*A* indicate peaks of density at radii of 176 and 204 Å, consistent with a bilayer width of 28 Å, and visible in the radial density profile (Fig. 3*D*). The strongest peak of protein density is found at a radius of 248 Å. There is a trough in the radial density profile between the peaks corresponding to protein and lipid, consistent with minimal contact between

the protein and lipid (arrow in Fig. 3*D*). To determine whether this minimum is an artifact of Fresnel fringe effects we applied an approximate correction for the CTF to the equatorial data in the Fourier transform after low-pass filtering. After this procedure the minimum between the protein and lipid peaks was still clearly visible.

The protein units making up the surface lattice can be seen in the cross-sectional view of the tube (Fig. 3*A*), with one marked in *magenta*; note the 6-fold symmetry of the cross-section, consistent with all layer lines having Bessel orders, n , that are integral multiples of six. A close-up view of the outer tube surface is shown in Fig. 3*B*. The protein repeating unit has 2-fold rotational symmetry, and has the size and shape of a dimer of heterotrimers, one of which is highlighted in *magenta* in Fig. 3. There are even more extensive contacts between adjacent heterotrimers in each helical strand, primarily made by the outermost parts of each molecule, across the *diagonal lines* drawn in Fig. 3*C*.

Protein and Lipid Contacts—A computationally isolated heterotrimer unit is shown in Fig. 4. Its lipid contacts can be seen in the side view of Fig. 4*A*. It is clear that each heterotrimer makes two strong contacts (*i.e.* ones that are still present when the density threshold is increased to enclose only 40% of the molecular volume) with central lipid; they are labeled *i* and *ii* in Fig. 4. To reveal how the protein is oriented on the membrane surface, the lipid was cut off so that the protein side of the protein-lipid interface can be seen (Fig. 4*B*) as viewed from the lipid surface. The two protruding “feet” (marked *i* and *ii*) correspond to the membrane binding portions of the protein. The surface areas of these contact regions are 390 and 125 Å². This total represents less than 2% of the 28,000 Å² total surface area of the protein as probed with a sphere of 4 Å radius.

Fitting the X-ray Structure of $G\alpha\beta\gamma_t$ into the EM Map—The single heterotrimer unit was computationally isolated by cut-

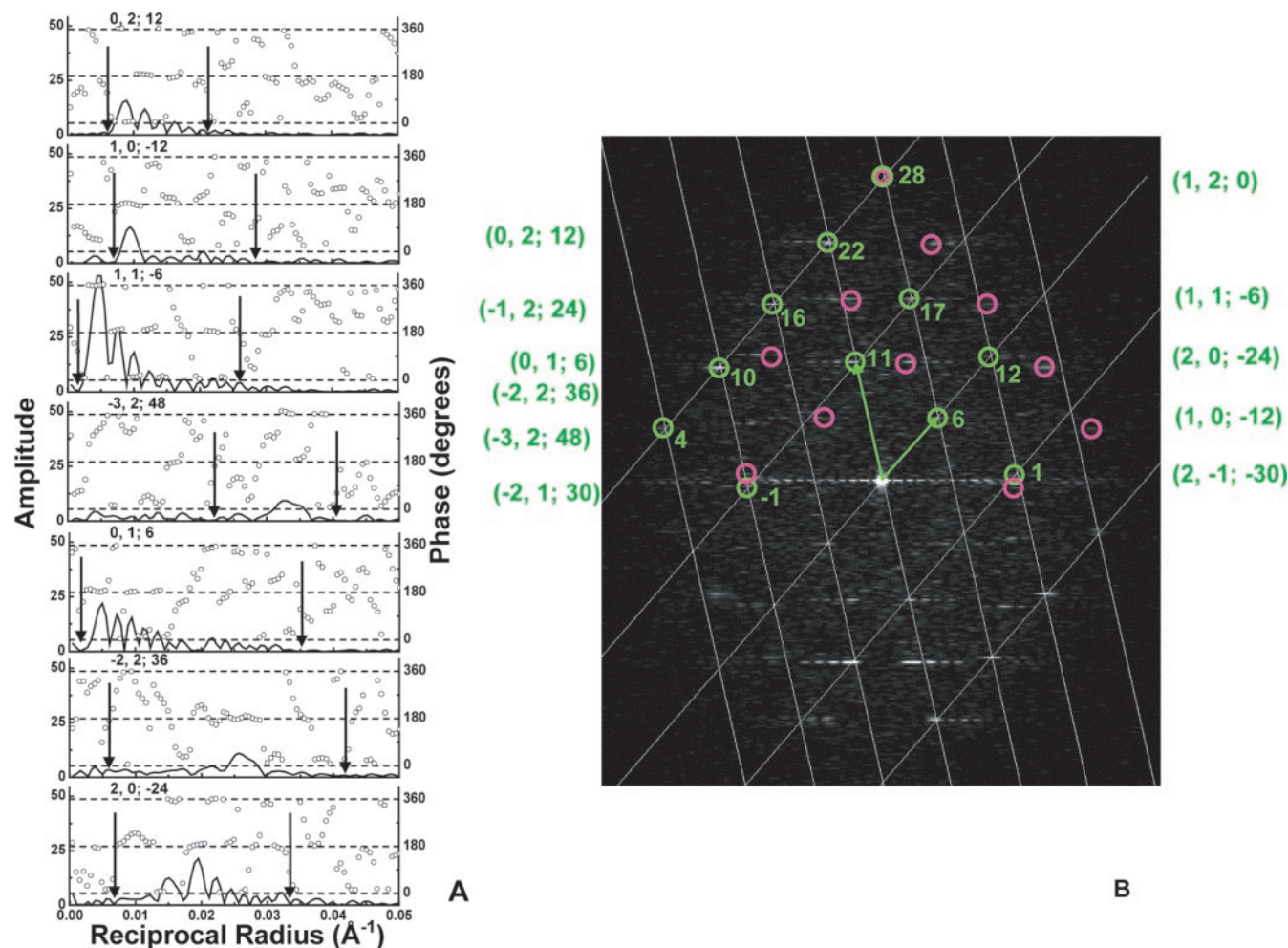


FIG. 2. **Layer line indexing.** A, amplitude and phase plots. The plots shown are averages from both sides of three tubes. *Solid lines*, radial amplitudes; *circles*, phases. The $(h, k; n)$ indices are given above each plot. The phases at amplitude maxima are close to either 0 (360°) or 180° indicating good 2-fold symmetry. *Arrows* indicate the ranges of data used, with the one at high resolution corresponding to the isotropic 23 Å resolution limit for each layer line height. B, surface lattice and indexing scheme. The h, k lattice is drawn and peak positions are identified by lattice position and Bessel order, n , as $(h, k; n)$ for layer lines arising from one side of the tube (green). Off-lattice peaks correspond to the lattice from the opposite side. Layer line numbers are indicated next to the circled peaks, and follow a selection rule of $l = tn + um$, where l is the layer line number, n is the Bessel order, t is the number of turns, -4 , u is the number of units in t turns, 7, and m is an integer.

ting with planes tangential to and perpendicular to the tube surface, as shown in Fig. 4, A and B. This unit was then used to obtain the best fit of the $G\alpha\beta\gamma_t$ x-ray crystal structure (16) using the program Foldhunter (23); the crystal structure at a resolution of 30 Å is shown in Fig. 4, C and D. The rough position of the structures is largely determined by the region of highest density, which is in the core of the β -propeller of $G\beta_t$. Optimizing the cross-correlation between the two structures yielded the alignment shown in Fig. 4, E and F. The aligned position of the crystal structure is shown in greater detail in Fig. 5. On a relative scale for the cross-correlation score of -1 to 1, the value for the optimal position is 0.45.

Fig. 4, E and F, shows side and bottom views of a portion of the EM map corresponding to a single heterotrimer, represented as a mesh surface, superimposed on a ribbon representation of the crystal structure in the best-fit orientation. The membrane surface lies on a horizontal plane just below the protein in Fig. 4E, and is parallel to and above the page in Fig. 4F. In this position the N-terminal helix of $G\alpha_t$ and its $\beta 2$ – $\beta 3$ loop are close to the membrane surface, and none of the regions of $G\beta_t$ and $G\gamma_t$ visible in the crystal structure are immediately adjacent to the membrane. The last visible residue on the C terminus of $G\gamma_t$, Glu⁶⁶ (the green terminus near the “i” in Fig. 4E), is positioned so that the missing residues 67–71, including

the farnesyl moiety on Cys⁷¹, could easily extend to the membrane surface. It is likely that the missing portions of the C terminus of $G\gamma_t$ and the N terminus of $G\alpha_t$, including their covalently attached lipids, make up most of the density connecting to the membrane at attachment site i shown on the left-hand side of Fig. 4E. The residues at attachment site ii, on the right-hand side of Fig. 4E, shown in closer detail in Fig. 5, A and B, appears to be those from the $G\alpha_t$ $\beta 2$ – $\beta 3$ loop, especially Lys¹⁸⁸ (yellow) and Asp¹⁸⁹ (purple), as well as Arg²⁸ (tan) from the C-terminal end of the N-terminal helix of $G\alpha_t$ (all color-coded residues are shown in ball and stick representation). The side chains of both Asp¹⁸⁹ and Arg²⁸ extend toward the membrane surface in this position, whereas that of Lys¹⁸⁸ points away from the membrane toward aspartate residues 333 and 337.

DISCUSSION

Restriction of Membrane Contacts to Two Narrow Surfaces—Perhaps the most surprising result from the reconstruction is that the area of contact between protein and lipid is quite small, involving only 2% of the protein surface. This conclusion follows from inspection of the map, and does not depend on the details of the fitting. It can actually be drawn simply from the radial density profile (Fig. 3D) prepared by back-transforma-

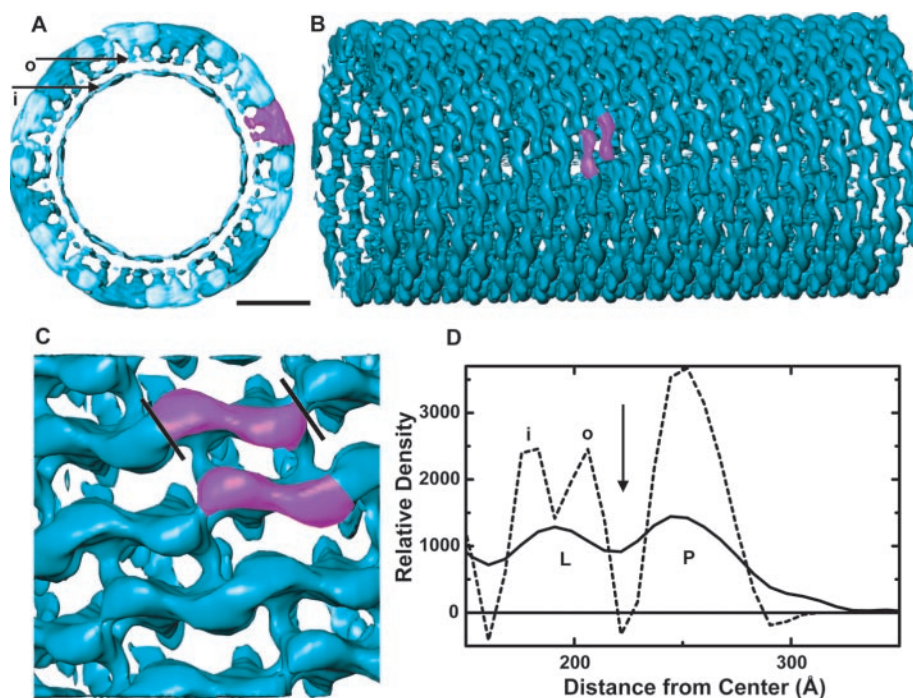


FIG. 3. **Helical reconstruction of G_t -lipid tubules.** The reconstruction shown was generated using merged data from three tubes of a single family illustrated in Figs. 1 and 2. *A*, cross-section of the reconstruction viewed down its long axis. *Inner* and *outer* arrows indicate the features interpreted as the inner (*i*) and outer (*o*) surfaces of the lipid head groups of the bilayer; noise in the center of the reconstruction is not shown. The magenta colored area represents one heterotrimer unit of the protein in the outer shell, including its contacts with the outer lipid head groups. Scale bar, 150 Å. *B*, side view, showing the surface lattice of G proteins. The magenta colored regions correspond to the repeating dimer of heterotrimers that make up the surface lattice. *C*, close-up view of the outer tube with a symmetry-related pair of heterotrimers highlighted. Two additional kinds of inter-heterotrimer contacts occur across the *black diagonal lines*. *D*, radial density plot before (*dashed lines*) and after (*solid line*) low-pass filtering and CTF correction. *L* and *P* mark the features interpreted as the lipid bilayer and peripherally bound protein, respectively. The features proposed to represent the inner and outer head groups of the lipid bilayer are labeled *i* and *o*, respectively; these are not resolved after the low-pass filtering used in the CTF correction. The *vertical arrow* indicates the minimum in the density corresponding to the region between the protein and the outer lipid head group, present both with and without CTF correction to reduce Fresnel fringe effects.

tion of the equatorial line in the Fourier transform, and therefore does not even depend on the accuracy of the reconstruction. A model proposed previously (16) for binding of G_t to the membrane, based on the crystal structure and electrostatic calculations, implied extensive interactions between the surfaces of the protein and the lipid. In contrast, the structure revealed by electron crystallography indicates very few direct contacts between the lipid surface and the protein, and the regions near the membrane surface are predominantly of negative charge (Fig. 6B).

Limited contact between protein and lipid surfaces is characteristic of a number of peripheral membrane proteins whose membrane interactions are known. EPR studies using site-specific spin labeling of the membrane-associated and lipid-hydrolyzing bee venom phospholipase A_2 demonstrated that only a small patch of residues directly contacts the membrane (44), and similar conclusions were reached by applying the same technique to a different peripheral protein, *Thermomyces lanuginosa* lipase (45). Recent calculations (46) for several phosphoinositide-binding FYVE domains predict minimal contact between the protein and membrane surfaces. Solid-state NMR studies of another fatty acylated peripheral membrane protein from photoreceptors, recoverin, also revealed membrane contacts largely limited to the lipid tail and immediately adjacent residues near the N terminus (47). Our structure illustrates what is likely a general principle of peripheral membrane protein binding to membranes: both the lipid head groups and the polar side chains found on protein surfaces interact strongly with water, and the energetic costs of eliminating these interactions upon forming polar membrane-protein contacts tend to preclude extensive protein-membrane con-

tacts, outside those specific contact points that confer high affinity. Minimal contacts between lipid and protein may also facilitate translocation of G_t that has been observed in response to strong illumination (48, 49).

Another unexpected finding is the close contact made by the $\beta 2$ - $\beta 3$ loop, likely in cooperation with the C-terminal residues missing in the x-ray structure, and arginine 28 from the C-terminal end of the N-terminal helix (*site ii* in Fig. 4). When the x-ray structure is fit into our membrane complex structure, the side chains of arginine 28 and aspartate 189 extend toward the lipid bilayer, and these are likely involved in polar contacts with lipid head groups. In the x-ray structure the $C\alpha$ position of lysine 188 is such that the side chain could easily extend toward the bilayer; however, in the crystal, the ϵ -amino group is sandwiched between the γ -carboxylates of aspartate 333 and aspartate 337, forming a salt bridge to aspartate 333. It is possible that when bound to negatively charged native membranes, these interactions could be replaced by interactions with the lipids. Interestingly, the $^{188}\text{KDL}^{190}$ sequence is conserved among all known rod and cone transducin α subunits.

Plasticity of the Membrane Binding Regions—It is possible that the position of the N-terminal α helix of G_{α_i} with respect to the rest of the heterotrimer is somewhat different when in membrane bound than in solution or in three-dimensional crystals. The orientation of this helix is different in some other G protein crystal structures, and too disordered to be resolved in most G_{α} structures. Fig. 5, *C* and *E*, show the dramatically different orientation of the N-terminal helix in the structure of G_{α_i} in complex with RGS4 (50); both of these orientations are likely different from the one used for membrane binding. Changes in position of the G_{α} N-terminal helix could be facil-

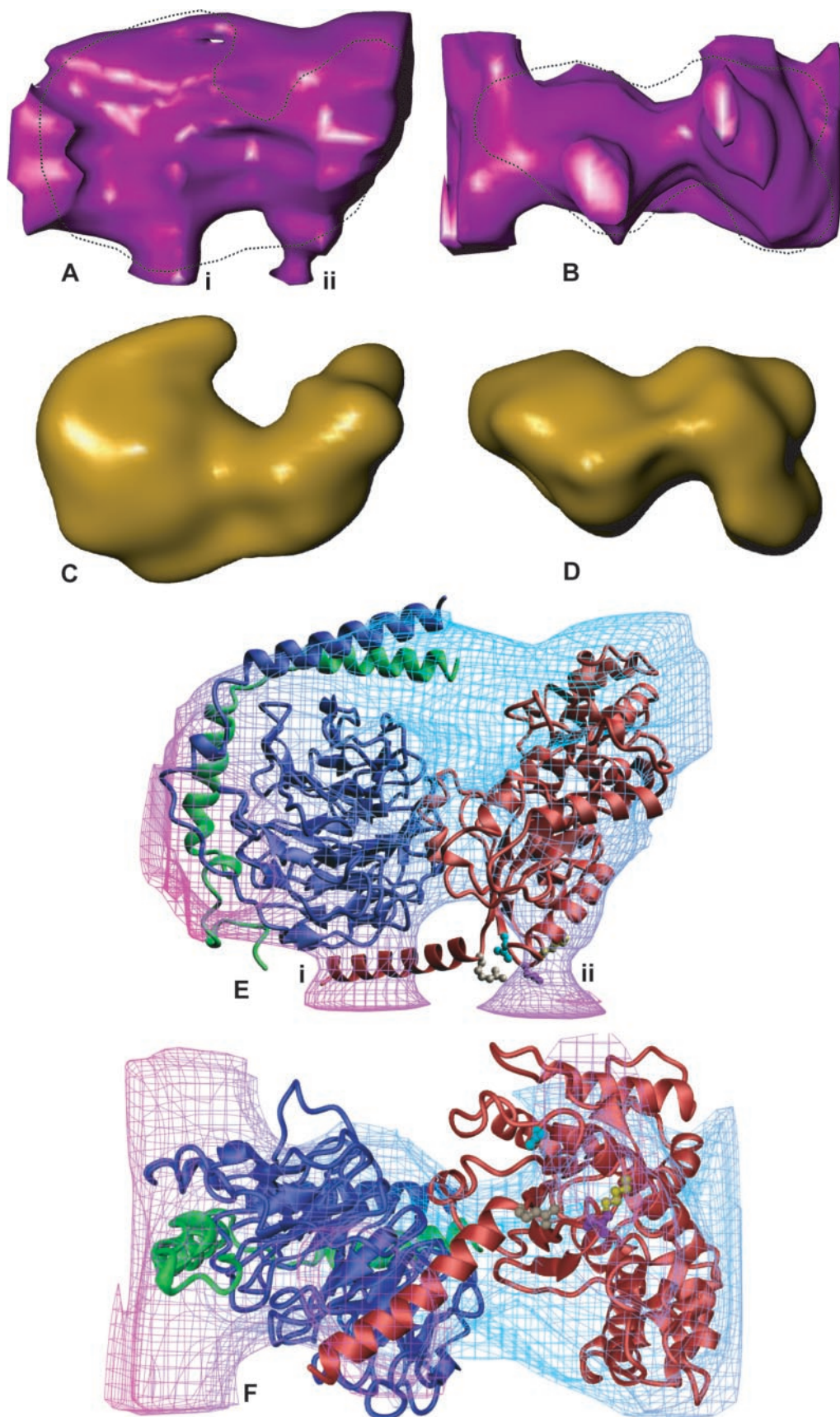


FIG. 4. **Fitting of x-ray structure of heterotrimer into membrane complex structure.** *A* and *B* show a side view and a view from the membrane surface, respectively, of an individual heterotrimer unit, corresponding to the *magenta* colored features in Fig. 3, cut at the narrowest points of membrane contact. The *dashed lines* indicate the outlines of the crystal structure at 30 Å resolution as shown in *C* and *D*. *E*, and *F* show side and bottom views, respectively, of the x-ray structure, in *ribbon* representation, fit into the membrane complex structure, shown as a transparent mesh corresponding to the surface enclosing 85% of the molecular volume. A spatial gradient of color is used to help identify corresponding portions of the surface in *panels E* and *F*. In *E*, the immediately adjacent region of the membrane surface is also shown. $G\alpha$ is shown

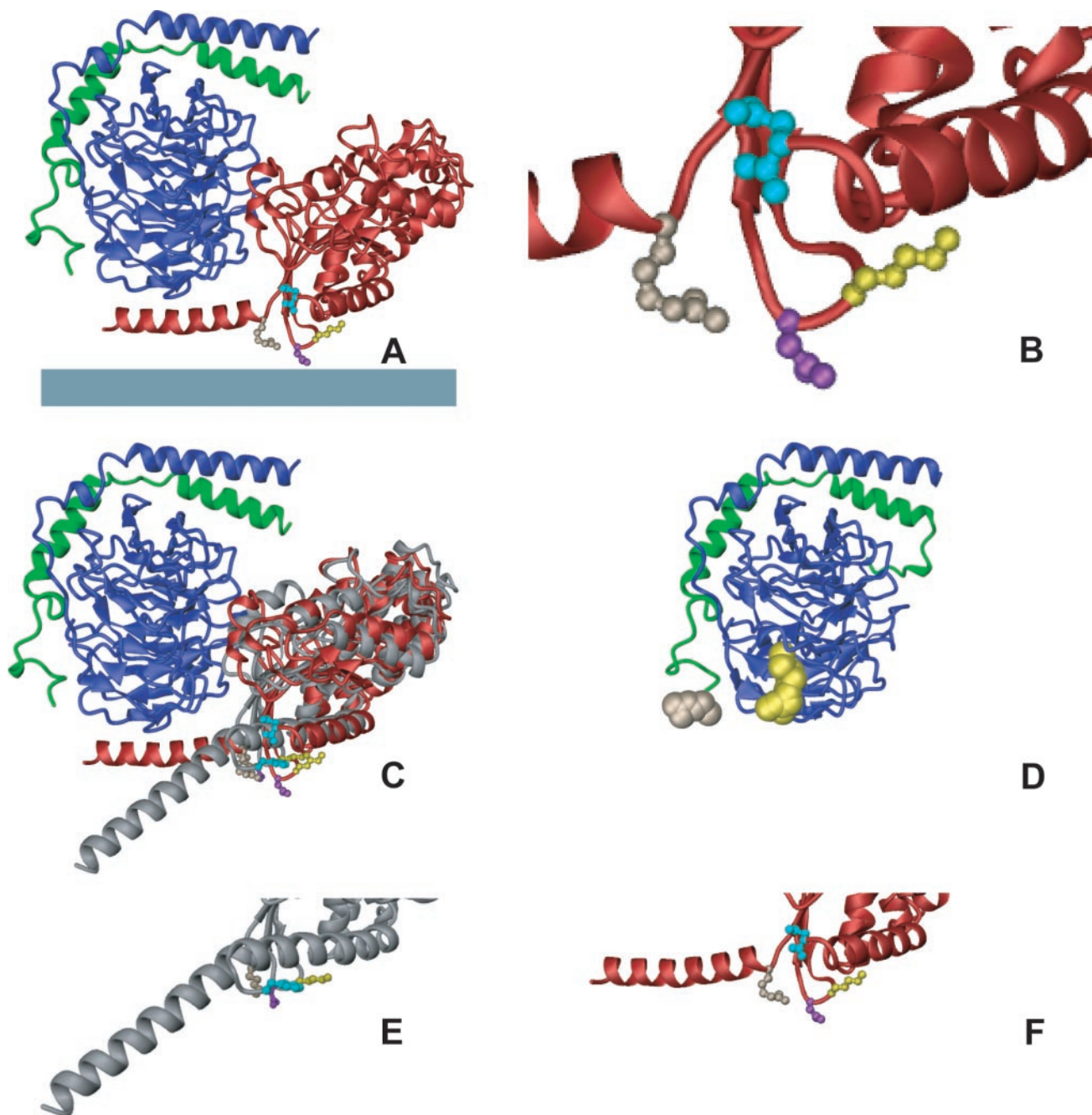


FIG. 5. **Plasticity of the membrane binding regions.** In *panels A and B*, the ribbon diagram of G_i from the heterotrimer structure (16) is shown oriented with respect to the membrane as determined from the fit to the EM reconstruction. The membrane is shown as a blue-gray bar. Of the $G\alpha$ residues visible in the x-ray structure, those closest to the membrane are shown in ball and stick representation: Arg²⁸, tan; Asp¹⁸⁹, purple; and Lys¹⁸⁸, yellow. The last visible residue at the C terminus of $G\alpha$, Asn³⁴³, is shown in cyan. It is followed by seven residues not visible in the crystal structure; the length of this missing segment is more than sufficient to reach the membrane surface. *Panel C* shows an alignment of a different $G\alpha$ structure, from the RGS4- $G\alpha_i$ -GDP- AlF_4^- complex (50). This alignment illustrates the potential mobility of the N-terminal helix and the C-terminal region; close-ups are shown in *panels E and F*. The same color coding is used for the identical near-membrane residues as in *panels A and B*, except that the last C-terminal residue in the $G\alpha_i$ structure, Phe³⁵⁵, corresponding to C-terminal Phe³⁵⁰ in $G\alpha_i$, is colored in cyan. This C-terminal residue would contact the membrane in this orientation. *Panel D* shows the structure of $G\beta\gamma_i$ from the phosducin complex (17) in the same orientation as the membrane bound form. In this structure the last $G\gamma$ C-terminal residue that is resolved is Glu⁶⁶, but the C-terminal farnesyl group attached to Cys⁷¹, is visible, and is shown in yellow. The four intervening residues could easily provide sufficient length for membrane insertion by the farnesyl group.

itated by electrostatic interactions between negatively charged lipid groups and the six basic residues (Lys¹⁰, Arg¹³, Lys¹⁷, Lys²⁰, Lys²⁵, and Arg²⁸) favorably positioned on the side near

the membrane surface. Not surprisingly, as can be seen in Fig. 4E, the fit of this part of the crystal structure is not as good as the rest, consistent with a somewhat different position in the

in red, $G\beta$ in blue, and $G\gamma$ in green. The green chain terminus near the letter (E) shows the last C-terminal $G\gamma$ residue visible in the crystal structure, which is followed by five residues and a covalently attached farnesyl group not seen in the x-ray structure. The N-terminal helix of $G\alpha$ is seen running nearly parallel to the membrane surface at the bottom of panel E. Also near the membrane surface in panel E is the last residue of the C terminus of $G\alpha$, visible in the crystal structure, shown in cyan ball and stick representation.

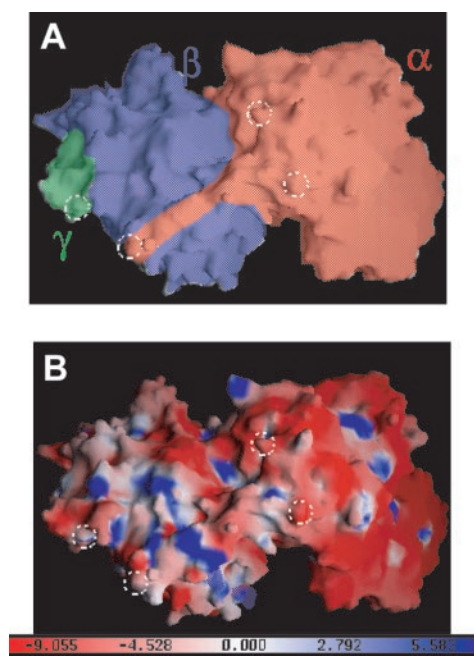


FIG. 6. The membrane binding surface of $G\alpha\beta\gamma$. Panel A shows a surface representation, as seen from the membrane surface, colored by subunit: $G\alpha$, red; $G\beta$, blue; $G\gamma$, green. Protuberances closest to the membrane are outlined with dashed circles. In panel B, the same surface representation is colored by electrostatic potential (scale in units of $k_B T$). The membrane contact points have negative or near neutral potentials, but there are somewhat more distant patches of positive potential on this surface that may act to reduce electrostatic repulsion. Surface representations and electrostatic calculations were prepared using GRASP (37).

membrane complex as opposed to its position in solution or in the three-dimensional crystal.

The same may be true for the farnesylated C terminus of $G\gamma$. Fig. 5D shows the position of the farnesyl group covalently attached to the C-terminal cysteine of $G\gamma_t$, in the one structure in which it is resolved (17), and found to be bound in a surface groove of $G\beta_t$. This structure is actually a complex of $G\beta\gamma_t$ with phosducin, which renders normally membrane-attached $G\beta\gamma_t$ soluble, so it is likely that in the membrane-attached form, this lipid moiety is inserted into the membrane, requiring large scale movement from the position shown in Fig. 5D. There is sufficient length of polypeptide chain plus the farnesyl group to reach the membrane at a site adjacent to the fatty acid attached to the N terminus of $G\alpha_t$, and the intervening sequence includes hydrophobic residue Leu⁶⁶ and the positively charged Lys⁶⁷. Likewise, the C terminus of $G\alpha_t$ seen in the RGS4 complex is in a position that could easily reach the membrane surface (Fig. 5, C and E). The missing C-terminal residues include one positive charge, Lys³⁴⁵, and three hydrophobic groups, Leu³⁴⁴, Leu³⁴⁹, and Phe³⁵⁰.

Functional Implications—The resting GDP-bound form of the G_t heterotrimer present in the crystals has as its major function recognition of photoexcited rhodopsin, R^* . Three features of the structure observed may assist in this function.

First, it is likely that the orientation of the protein with respect to the lipid surface is close to the orientation with respect to the cytoplasmic surface of rhodopsin that is used in forming the $G\alpha\beta\gamma_t R^*$ complex. The N terminus of $G\alpha_t$, and its C terminus, which are positioned close to the membrane surface in the reconstruction, have been implicated in R^* binding, as has the C terminus of $G\gamma$ (51, 52). Addition of an ADP-ribose group by pertussis toxin at position cysteine 344, the fourth residue from the C terminus of $G\alpha_t$, abolishes R^* interactions without affecting spontaneous nucleotide exchange or hydroly-

ysis (53). Cross-linking of R^* to $G\alpha\beta\gamma_t$ yielded primarily cross-links to residues in the C-terminal region of $G\alpha$ (54), and mutagenesis and peptide studies support an important role for the C terminus of $G\alpha$ (18, 19). All these regions are positioned near the membrane surface in our structure.

Second, the limited areas of contact between membrane and protein allow for conformational and positional flexibility. It seems likely that there is considerable motion of $G\alpha\beta\gamma_t$ about the average position found in the reconstruction, because of the paucity of constraints from membrane interactions. Thus $G\alpha\beta\gamma_t$ is able to sample many different orientations rapidly in its search for photoexcited rhodopsin, which it may encounter from many different directions as a consequence of two-dimensional diffusion, freely rotating in the plane of the membrane and also toward and away from the membrane surface.

Third, very little of the surface of $G\alpha\beta\gamma_t$ is masked by the membrane. Although we do not yet know precisely the structure of the interface between R^* and $G\alpha\beta\gamma_t$, it seems likely that it occupies much of the surface area of the cytoplasmic loops of rhodopsin. The scarcity of lipid contacts allows easy access of the R^* surface to that of $G\alpha\beta\gamma_t$.

Links between Heterotrimers—It is unclear whether the extensive contacts each G_t makes with neighboring heterotrimers in each strand and across the 2-fold symmetry axis represent physiologically relevant complexes, or are induced by our crystallization conditions. There is evidence from cross-linking and other studies that under certain conditions G_t can form dimers or multimers (55–58). Atomic force microscopy of photoreceptor membranes indicates that rhodopsin can form rows of dimers (59, 60), implying that G_t may interact with R^* as a dimer or higher order complex. Recent photobleaching recovery experiments in transgenic *Xenopus* rods² support the notion that $G_t R^*$ participates in a very slowly diffusing multimeric complex *in vivo*. It is not clear whether conditions in rod outer segments would be conducive to formation of $G_t G_t$ complexes, because while the concentration of G_t inside the rod outer segment is actually more than 200-fold higher than the sub-phase concentration we used for crystallization, the average surface density is lower than in our helical lattice.

Relationship to Structure on Photoreceptor Membranes—Two features of the environment of the structure presented here differ substantially from *in vivo* conditions: the assembly of a lattice completely covering the membranes, and the presence of an unnatural mix of lipids. Several control experiments and lines of reasoning suggest that the interactions with the membrane seen here closely resemble functional interactions inside the cell. First, we have verified that the lipids used in crystallization support the conformational change in G_t induced by the transition state analogue, GDP-AlF₄ (28), even in the crystalline lattice. Moreover, the same lipids support very efficient activation of the natural effector enzyme PDE6 (27, 61). The observation that similar helical lattices form on tubes composed of endogenous rod outer segment lipids present in partially purified G_t (28) further support the notion that the membrane complex we observe is unlikely to be drastically different from one formed on native membranes. There are, of course some uncertainties in the higher resolution features of our reconstruction and the fitting in of the x-ray structure. However, the basic conclusions about which parts of the protein are near the membrane also hold true for other fits with slightly worse scores as well as for the best fit shown here, because these have the same basic orientation. The conclusion about a narrow area of contact between the lipids and protein does not depend on the details of the reconstruction and fitting at all.

² X. Zhang and T. Wensel, unpublished observations.

Finally, there is excellent agreement between the regions of the protein we identify as interacting with the membranes and biochemical data on the role of lipid modifications and on the role in R* binding of the C-terminal. All of these considerations argue that if the orientation we observe with respect to the membrane is not the one that is primarily occupied *in vivo*, it is almost certainly one that is occupied a significant fraction of the time. Because the structure and fit make strong predictions about the roles of individual residues, they can be readily tested by techniques of mutagenesis and transgenesis.

Future Expectations—The power of electron cryo-microscopy and electron crystallography for studying membrane-dependent signaling complexes is only just beginning to be realized. In this study we have determined the structure of the membrane complex formed by the G protein heterotrimer alone. The phototransduction system may provide a useful source of substrates for determination of additional structures of signaling complexes using electron cryo-microscopy. At the membrane surface, G_i interacts with rhodopsin, the peripheral membrane protein cGMP phosphodiesterase (PDE6), and the GTPase accelerating complex of RGS9-1, Gβ_{5L}, and R9AP. All of these complexes can be readily reconstituted on membranes from purified components for structural analysis, and serve as models for understanding similar complexes of G proteins formed with receptors, effectors, and RGS proteins in nearly all eukaryotic cells.

Acknowledgments—We thank Drs. S. Ludtke, W. Jiang, M. Baker, and M. Sowa for helpful suggestions and assistance.

REFERENCES

- Brand, S. H., Holtzman, E. J., Scher, D. A., Ausiello, D. A., and Stow, J. L. (1996) *Am. J. Physiol.* **270**, C1362–C1369
- Busconi, L., Boutin, P. M., and Denker, B. M. (1997) *Biochem. J.* **323**, 239–244
- Chen, C. A., and Manning, D. R. (2001) *Oncogene* **20**, 1643–1652
- Fukada, Y. (1995) *Methods Enzymol.* **250**, 91–105
- Matsuda, T., Hashimoto, Y., Ueda, H., Asano, T., Matsuura, Y., Doi, T., Takao, T., Shimonishi, Y., and Fukada, Y. (1998) *Biochemistry* **37**, 9843–9850
- Sanford, J., Codina, J., and Birnbaumer, L. (1991) *J. Biol. Chem.* **266**, 9570–9579
- Yamane, H. K., Farnsworth, C. C., Xie, H. Y., Howald, W., Fung, B. K., Clarke, S., Gelb, M. H., and Glomset, J. A. (1990) *Proc. Natl. Acad. Sci. U. S. A.* **87**, 5868–5872
- Lai, R. K., Perez-Sala, D., Canada, F. J., and Rando, R. R. (1990) *Proc. Natl. Acad. Sci. U. S. A.* **87**, 7673–7677
- Fukada, Y., Takao, T., Ohguro, H., Yoshizawa, T., Akino, T., and Shimonishi, Y. (1990) *Nature* **346**, 658–660
- Fukada, Y., Matsuda, T., Kokame, K., Takao, T., Shimonishi, Y., Akino, T., and Yoshizawa, T. (1994) *J. Biol. Chem.* **269**, 5163–5170
- Parish, C. A., Smrcka, A. V., and Rando, R. R. (1995) *Biochemistry* **34**, 7722–7727
- Parish, C. A., and Rando, R. R. (1996) *Biochemistry* **35**, 8473–8477
- Dietrich, A., Brazil, D., Jensen, O. N., Meister, M., Schrader, M., Moomaw, J. F., Mann, M., Illenberger, D., and Gierschik, P. (1996) *Biochemistry* **35**, 15174–15182
- Myung, C. S., Yasuda, H., Liu, W. W., Harden, T. K., and Garrison, J. C. (1999) *J. Biol. Chem.* **274**, 16595–16603
- Wall, M. A., Coleman, D. E., Lee, E., Iniguez-Lluhi, J. A., Posner, B. A., Gilman, A. G., and Sprang, S. R. (1995) *Cell* **83**, 1047–1058
- Lambright, D. G., Sondke, J., Bohm, A., Skiba, N. P., Hamm, H. E., and Sigler, P. B. (1996) *Nature* **379**, 311–319
- Loew, A., Ho, Y. K., Blundell, T., and Bax, B. (1998) *Structure* **6**, 1007–1019
- Garcia, P. D., Onrust, R., Bell, S. M., Sakmar, T. P., and Bourne, H. R. (1995) *EMBO J.* **14**, 4460–4469
- Hamm, H. E., Rarick, H., Mazzoni, M., Malinski, J., and Suh, K. H. (1990) *Biochem. Soc. Symp.* **56**, 35–44
- Kuhn, H. (1980) *Nature* **283**, 587–589
- Stryer, L., Hurley, J. B., and Fung, B. K. (1983) *Methods Enzymol.* **96**, 617–627
- Seitz, H. R., Heck, M., Hofmann, K. P., Alt, T., Pellaud, J., and Seelig, A. (1999) *Biochemistry* **38**, 7950–7960
- Jiang, W., Baker, M. L., Ludtke, S. J., and Chiu, W. (2001) *J. Mol. Biol.* **308**, 1033–1044
- Wu, X., Milne, J. L., Borgnia, M. J., Rostapshov, A. V., Subramaniam, S., and Brooks, B. R. (2003) *J. Struct. Biol.* **141**, 63–76
- Rossmann, M. G., Bernal, R., and Pletnev, S. V. (2001) *J. Struct. Biol.* **136**, 190–200
- Chacon, P., and Wriggers, W. (2002) *J. Mol. Biol.* **317**, 375–384
- Melia, T. J., Malinski, J. A., He, F., and Wensel, T. G. (2000) *J. Biol. Chem.* **275**, 3535–3542
- Melia, T. J., Sowa, M. E., Schutze, L., and Wensel, T. G. (1999) *J. Struct. Biol.* **128**, 119–130
- Fukami, A., and Adachi, K. (1965) *J. Electron Microsc.* **14**, 112–118
- Toyoshima, C. (1989) *Ultramicroscopy* **30**, 439–444
- Avila-Sakar, A. J., and Chiu, W. (1996) *Biophys. J.* **70**, 57–68
- Ludtke, S. J., Baldwin, P. R., and Chiu, W. (1999) *J. Struct. Biol.* **128**, 82–97
- Schmid, M. F., Dargahi, R., and Tam, M. W. (1993) *Ultramicroscopy* **48**, 251–264
- DeRosier, D. J., and Moore, P. B. (1970) *J. Mol. Biol.* **52**, 355–369
- Dougherty, M. T., and Chiu, W. (1998) *Microsc. Microanal.* **4**, 452–453
- Berman, H. M., Westbrook, J., Feng, Z., Gilliland, G., Bhat, T. N., Weissig, H., Shindyalov, I. N., and Bourne, P. E. (2000) *Nucleic Acids Res.* **28**, 235–242
- Nicholls, A., Sharp, K. A., and Honig, B. (1991) *Proteins* **11**, 281–296
- DeRosier, D., Stokes, D. L., and Darst, S. A. (1999) *J. Mol. Biol.* **289**, 159–165
- Toyoshima, C., and Unwin, N. (1990) *J. Cell Biol.* **111**, 2623–2635
- Zhang, P., Toyoshima, C., Yonekura, K., Green, N. M., and Stokes, D. L. (1998) *Nature* **392**, 835–839
- Polyakov, A., Severinova, E., and Darst, S. A. (1995) *Cell* **83**, 365–373
- Ludtke, S., Sasabe, H., and Stokes, D. L. (1993) *Nature* **362**, 467–471
- Akiba, T., Toyoshima, C., Matsunaga, T., Kawamoto, M., Kubota, T., Fukuyama, K., Namba, K., and Matsubara, H. (1996) *Nat. Struct. Biol.* **3**, 553–561
- Lin, Y., Nielsen, R., Murray, D., Hubbell, W. L., Mailer, C., Robinson, B. H., and Gelb, M. H. (1998) *Science* **279**, 1925–1929
- Hedin, E. M., Hoyrup, P., Patkar, S. A., Vind, J., Svendsen, A., Fransson, L., and Hult, K. (2002) *Biochemistry* **41**, 14185–14196
- Diraviyam, K., Stahelin, R. V., Cho, W., and Murray, D. (2003) *J. Mol. Biol.* **328**, 721–736
- Valentine, K. G., Mesleh, M. F., Opella, S. J., Ikura, M., and Ames, J. B. (2003) *Biochemistry* **42**, 6333–6340
- Sokolov, M., Lyubarsky, A. L., Strissel, K. J., Savchenko, A. B., Govardovskii, V. I., Pugh, E. N., Jr., and Arshavsky, V. Y. (2002) *Neuron* **34**, 95–106
- Whelan, J. P., and McGinnis, J. F. (1988) *J. Neurosci. Res.* **20**, 263–270
- Tesmer, J. J., Berman, D. M., Gilman, A. G., and Sprang, S. R. (1997) *Cell* **89**, 251–261
- Kisselev, O. G., Meyer, C. K., Heck, M., Ernst, O. P., and Hofmann, K. P. (1999) *Proc. Natl. Acad. Sci. U. S. A.* **96**, 4898–4903
- Jian, X., Clark, W. A., Kowalak, J., Markey, S. P., Simonds, W. F., and Northup, J. K. (2001) *J. Biol. Chem.* **276**, 48518–48525
- Ramdas, L., Disher, R. M., and Wensel, T. G. (1991) *Biochemistry* **30**, 11637–11645
- Cai, K., Itoh, Y., and Khorana, H. G. (2001) *Proc. Natl. Acad. Sci. U. S. A.* **98**, 4877–4882
- Hingorani, V. N., Tobias, D. T., Henderson, J. T., and Ho, Y. K. (1988) *J. Biol. Chem.* **263**, 6916–6926
- Wessling-Resnick, M., and Johnson, G. L. (1987) *J. Biol. Chem.* **262**, 12444–12447
- Wessling-Resnick, M., and Johnson, G. L. (1989) *Biochem. Biophys. Res. Commun.* **159**, 651–657
- Vaillancourt, R. R., Dhanasekaran, N., Johnson, G. L., and Ruoho, A. E. (1990) *Proc. Natl. Acad. Sci. U. S. A.* **87**, 3645–3649
- Fotiadis, D., Liang, Y., Filipek, S., Saperstein, D. A., Engel, A., and Palczewski, K. (2003) *Nature* **421**, 127–128
- Liang, Y., Fotiadis, D., Filipek, S., Saperstein, D. A., Palczewski, K., and Engel, A. (2003) *J. Biol. Chem.* **278**, 21655–21662
- Malinski, J. A., and Wensel, T. G. (1992) *Biochemistry* **31**, 9502–9512